

Research Article

Magnesium Oxide in Nanodimension: Model for MRI and Multimodal Therapy

M. Waseem Akram ¹, **Muhammad Fakhar-e-Alam** ^{1,2}, **Alvina Rafiq Butt** ³, **T. Munir**,²
Akbar Ali,⁴ **K. S. Alimgeer** ⁵, **Khalid Mehmood-ur-Rehman** ⁶, **Seemab Iqbal**,²
Salamat Ali,³ **Muhammad Ikram**,³ **N. Amin**,² and **Zhiming M. Wang** ¹

¹Institute of Fundamental and Frontier Science, University of Electronic Science and Technology of China, Chengdu 610054, China

²Department of Physics, Government College University, Faisalabad 38000, Pakistan

³Physics Department, Government College University (GCU), Lahore 54000, Pakistan

⁴Department of Physics, COMSATS Institute of Information Technology, Lahore 54000, Pakistan

⁵Department of Electrical Engineering, COMSATS Institute of Information Technology, Islamabad, Pakistan

⁶School of Physics & Material Sciences, Anhui University, Hefei, China

Correspondence should be addressed to M. Waseem Akram; waseem.physicist@gmail.com,
Muhammad Fakhar-e-Alam; fakharphy@gmail.com, Alvina Rafiq Butt; alvinarafiq@gcu.edu.pk,
and Zhiming M. Wang; zhmwang@gmail.com

Received 28 July 2017; Revised 15 January 2018; Accepted 19 March 2018; Published 20 June 2018

Academic Editor: Sherine Obare

Copyright © 2018 M. Waseem Akram et al. This is an open access article distributed under the Creative Commons Attribution License, which permits unrestricted use, distribution, and reproduction in any medium, provided the original work is properly cited.

The prime focus of this investigation is to determine which morphology of magnesium oxide (MgO) is nontoxic and accumulates in sufficient quantity to a human brain cellular/tissue model. Thus, nanostructured MgO was synthesized from a coprecipitation technique involving twin synthetic protocols and the resulting product was characterized by scanning electron microscopy (SEM), transmission electron microscopy (TEM), size distribution histogram, Fourier-transform infrared spectroscopy (FTIR), and X-ray diffraction (XRD) analysis and elemental composition was confirmed by EDX analysis. They were tested for selective antigen response in a human brain cancer model through biodistribution, biotoxicity via MTT assay, and tissue morphology. In addition, the MRI compatibility of MgO nanostructures and immunofluorescence studies were investigated on nanoconjugates with different immunoglobulins in the brain section. The results indicated that MgO had some degree of bindings with the antigens. These results led to the empirical modeling of MgO nanomaterials towards toxicity in cancer cells by analyzing the statistical data obtained by experiments. All these results are providing new rational strategy with the concept of MgO for MRI and PTT/PDT.

1. Introduction

Since the last decades, the nanostructure form of magnesium oxide (MgO) is actively involved in the field of science and technology due to extensive applications in catalysis and biomedicine serves as a biocompatible coverage for many drug vehicle formations towards an in vitro/in vivo model, even significant localization/uptake in blood vessels without clotting, improving the visibility of a specific organ in the outcome of very low concentration. Self-assembled MgO/Fe is a very

inspiring material for the MRI contrast agent. Furthermore, Fe NPs is very promising towards photothermal therapy, for example, hyperthermia mechanism after relevant light irradiation. After literature survey, dynamic MgO enhancement for MRI purpose is more suitable for acute group retroperitoneal fibrosis relative to chronic group fibrosis. For drug delivery and magnetic-activated cell storing application, MgO acts as a milestone and participates very actively in the biomedical field. Nature always favors the living organism, but sometimes, misuse of natural or miracle drugs has steered to

drug-resistant bacteria, which is one of the formidable challenges for healthcare practitioners. The major flaw of conventional therapies is nonsignificant bioavailability of drugs towards targeted sites [1–7].

The revolution of nanotechnology has driven many successful and innovative techniques including overwhelming deficiency of bioavailability of useful drugs, to enhance interaction between the nanoparticles and the microorganism, to overcome hindrance of multidrug resistance. The advancement of effective nanoparticles needs an in-depth study for the physicochemical response of developed NPs and biological features of microorganisms and risk factor related to a respective nanomaterial for safety evaluation as well [7, 8]. Gadolinium (Gd) and iron oxide nanoparticles (IONPs) due to their outstanding properties gained a privileged place in biomedical fields. For cancer detection, especially, IONPs have been greatly employed as contrast agents in magnetic resonance imaging (MRI) and photothermal therapy, because of their low side effects, inhibiting metastasis and overcoming multidrug resistances (MDR) [9, 10]. Along with several advantages, Gd might be toxic due to some specific sites especially used as a contrast agent for kidney and ischemia patients. Gadolinium-based contrast agents (GBCAs) are approved by the FDA for a better and improved form of body organs and tissue information associated with MRI. Gd having many advantageous features for cancerous patients also alarming for kidney and heart relevant patients, as nephrotoxic effects within a range of the same doses, is still debatable [11–15].

Some published data demonstrate encouraging results about the bioactivity of various drugs and antimicrobial formulations of certain materials (iron, gold, silver, zinc, manganese, etc.) as nanoparticles [16–18]. To the best of our knowledge, nanoMgO as compared to copper, silver, TiO_2 , and different types of bactericides exhibits an efficient biocidal, sporicidal, and antiviral activity [19–22]. Due to a high research track record, n-MgO has gained an outstanding property privilege place in biomedical fields very shortly and acquired attention of biomedical researchers [23].

Magnesium-based oxide materials (MgO , $\text{Mg}(\text{OH})_2$) are the exceptional candidates due to extensive applications in catalysis and anticancerous and antibacterial materials [7, 8, 24]. The hybrid form of magnetic nanoparticles (complexes of dendrimers etc.) has been opening a new horizon in the area of biomedical sciences. For the confirmation of the hybrid form and relevant investigation, many successful experiments were conducted in this context by applying assessment analysis of zeta potential, cell viability, cellular internalization, and lipid oxidation test for an NIH 3T3 cell model [25]. Lipid assembled for combined chemotherapy is very convincing and up to the marking technique, but PDT/PTT is more favorable due to less invasiveness. This form of lipid/nanoparticle is capable to enhance the localization of drug (doxorubicin) has toxicity, but the advantage is high accumulation into nuclei [26].

In this article, successful fabrication of nanosized magnesium oxide (n-MgO) via chemical precipitation route was attempted for the first time, which is nontoxic, most reliable, facile, up to the mark, novel, economical, and very amazing

ultrasmall nanoparticles and environmentally benign. Their cellular responses and molecular conjugation with specific antigens were also investigated on a cell/rat model. Figure 1 shows the schematic illustration of n-MgO-based photodynamic therapy in a cellular/mouse model and its trends towards MRI applications as well.

2. Experimental Procedures

2.1. Materials. All the chemical reagents magnesium chloride (MgCl_2), sodium hydroxide (NaOH), polyvinyl alcohol (PVA), and ethanol used in this experiment were purchased from Sigma-Aldrich.

2.2. Synthesis of MgO Nanotubes. Two separate transparent mixtures of MgCl_2 and NaOH were prepared in 50 ml of distilled water. MgCl_2 mixture was slowly dripped in NaOH solution (1 : 2) under constant stirring at 60°C through a volumetric burette. This reaction process was completed within 1 hour and kept at room temperature for an additional 1 hour to settle milky suspension of magnesium hydroxide ($\text{Mg}(\text{OH})_2$). This subsequent precursor was repetitively filtered and washed in water and ethanol, individually, to remove soluble impurities in the final product. This final product was vacuum dried at 60°C for overnight. The dried product was monitored through differential scanning calorimeter (DSC)/thermogravimetric (TG) to find the temperature at which $\text{Mg}(\text{OH})_2$ decomposes into MgO. After thermal analysis, the dried MgO powder was calcined at 350°C for 2 hours for further study. Similarly, MgO nanostructures were prepared by adopting the same route at different annealing temperatures (250°C and 350°C).

2.3. Characterization of Synthesized Nanopowder. The phase angle, crystal purity, and average crystallite size were determined by documenting data from X-ray diffraction (XRD, PAN X'Pert PRO, $\text{Cu-K}\alpha$ $\lambda = 1.5406 \text{ \AA}$). The morphology and particle size were calculated using a JEOL 6480LV scanning electron (SE) and a JEM 1230 transmission electron (TE) microscope. For TEM studies, MgO nanopowder was ultrasonically dispersed in acetone for 30 min. A few droplets of this solution were collected at a carbon-coated Cu grid and dried up in vacuum. Elemental analysis was carried through an energy dispersive X-ray analyzer (EDX) while a SHIMADZU Prestige 21 Fournier transformation Infra-red (FTIR) spectrometer was operated between 300 and 600 cm^{-1} at room temperature to detect the molecular structure of the synthesized product. An InVia Reflex Raman microscope (Renishaw) was operated at an excitation wavelength of 785 nm to confirm the crystalline nature of MgO. Photoluminescence spectrum was studied at an excitation wavelength of 350 nm using Fluorolog spectrometer fluorescence (Horiba Instruments, FL3-111 model).

2.4. Intracellular Distribution of MgO Nanotubes

2.4.1. Biological Materials. The stabilization process was performed by dissolving MgO nanopowder (1 g/w) and polyvinyl alcohol (2% (w/v)) in distilled water (98 ml) under constant stirring and heating at 55°C for 12 hours [27].

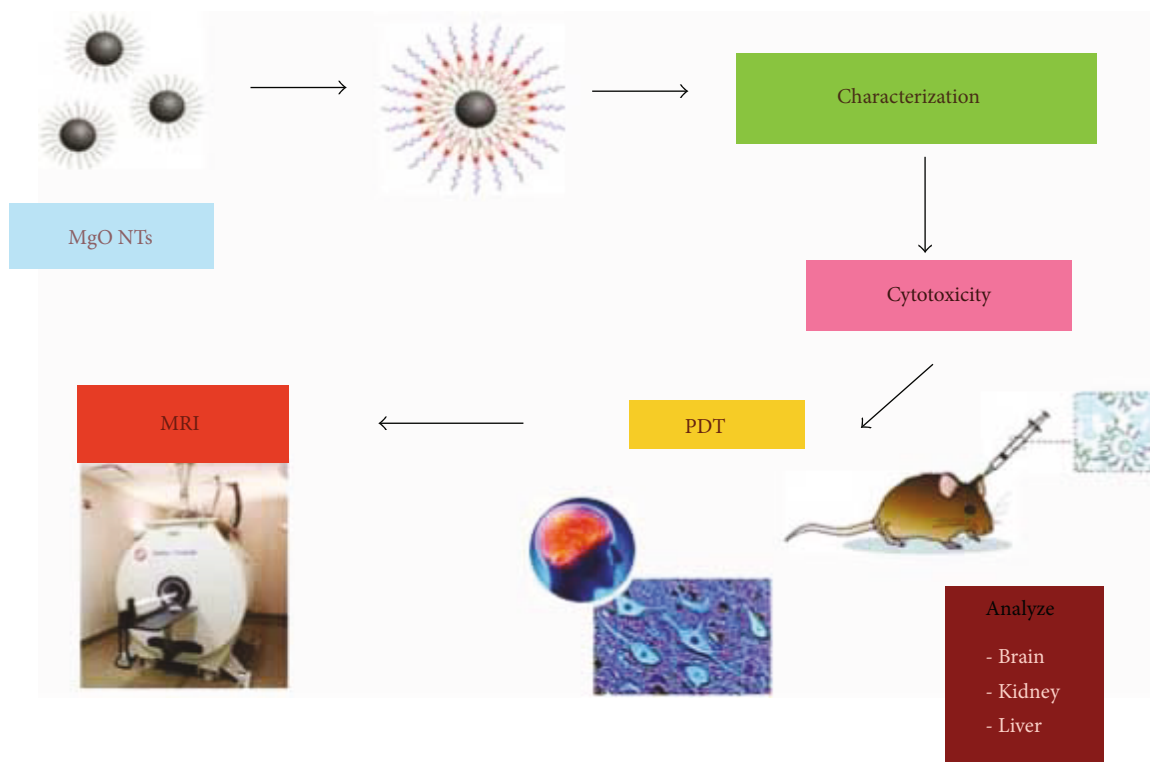


FIGURE 1: Schematic diagram of MgO applications towards PDT and MRI applications.

Subsequently, PVA-stabilized MgO nanosuspension was ready for intracellular distribution and for conjugation with different antibodies on rat brain tissues.

2.4.2. Ethical Approval. All the procedures including animal subjects and cell lines were accomplished under the UK Animal (Scientific Procedures) Act 1986 and had been approved by the Ethical Review Panel of the University of Cambridge with a recommendation of a minimum number of animals used for purposive results.

2.4.3. Animals. Ten male spontaneous hypertensive (SH) rats, 5 weeks old, were divided equally into two groups: A and B ($n = 5$), to carry out this research study. All the animals were kept in individual ventilated cages and had given ad libitum approach to distilled water and laboratory food at standard temperature (32°C).

2.4.4. Distribution Analysis. Each rat belonging to group A was injected subcutaneously with a single dose of $150\ \mu\text{l}$ of PVA-stabilized MgO nanofluid and put back to their cages under frequent observations for three months for any clinical toxic symptoms. After completion of investigation, the experiment was terminated by intraperitoneal (IP) sacrifice of rats administering sodium pentobarbitone ($30\ \text{mg}/100\ \text{g}$). Animals were positioned in the supine position on a perfusion table, and midline incision was made to open the thorax. A perfusion needle was passed from the left ventricle to the aorta, and it was secured. An incision was made to the right atrium to infuse using physiological saline ($\text{pH} = 7.4$, 4°C) till the fluid coming out of the right atrium was clear. The animals

were decapitated after perfusion with 4% paraformaldehyde (PFA) ($150\text{--}200\ \text{ml}$, $\text{pH} = 7.4$) solution. The brains were post-fixed in 4% PFA ($\text{pH} = 7.4$) after removing from the cranium free of olfactory bulbs overnight (4°C) and then dipped into 30% sucrose solution for cryoprotection [27, 28].

The skin, muscle, brain, kidney, and liver were detached and fixed in neutral phosphate-buffered formalin (10% (v/v)) for 24 hours and then preserved in paraffin blocks [27–29]. Pathological studies were made following standard procedures. Preserved sections were hydrated in graded concentrations of ethanol and stained with hematoxylin and eosin. After hydration and washing in Triton X-100 in Trizma base solution (TXTBS), the stained sections were fixed onto glass slides using DPX mount (1330-20-7, Merck) for microscopic analysis. An Olympus BX61 series system microscope at 200x magnifications was used to acquire images scanned on an Ariol SL 50 (Applied Imaging, Santa Clara, USA) [27].

2.5. Cell Culturing and Labelling Condition. Human glioblastoma cell line T98G was cultured at 37°C ; a 5% CO_2 -humidified environment was grown in Dulbecco's modified Eagle's medium (DMEM) supplemented with 10% fetal bovine serum (FBS) during culturing condition and 2% FBS during experimentation. In addition, DMEM was supplemented with 1% Na-pyruvate and 1% non-essential amino acids. The solution contains 5000 units/ml penicillin and 5000 microgram/ml of streptomycin as antibiotics supplement. All of the growth media and supplement were obtained from Sigma-Aldrich Company Ltd., China Mainland.

The experimental scheme of cell labelling is described very up to the mark. 96-well plates were preferred for subculturing and experimentation. In group I, five wells in each row were labelled/specified for each concentration of MgO dispersed solution (concentration range 0–250 $\mu\text{g}/\text{ml}$). The last two columns remained as control/reference (without any treatment). In group II, the same experimental protocol was repeated except 10–80 J/cm^2 of 660 nm of laser exposure. The time of incubation for cell localization was selected as 6, 24, and 48 hours. Cell viability of each well was assessed by applying MTT Assay [30, 31].

2.6. Conjugation of MgO Nanostructures with Antibodies

2.6.1. Induction of Middle Cerebral Artery Occlusion (MCAo).

All the rats belonging to group B underwent a surgical procedure to occlude temporarily MCA for 15 min and set them free back to the cages. After 91 days, brain MRI was performed to observe any inflammation/lesion produced as a result of 15 min occlusion before the execution of rats. The animals were sacrificed to collect the brain for immunofluorescence (IF) studies.

The methodology adopted for animal preparation, surgical procedure for tMCAo, MRI and IF investigation for neuronal loss (using a neuronal nuclear antigen NeuN), active microglia (a CD11b/c marker OX42), and astrocytes (glial fibrillary acidic protein GFAP) were the same as in the past investigations [27, 28]. The following method was discussed in brief.

2.6.2. Anesthesia and Physiological Monitoring. Two hours prior to surgery, buprenorphine (0.03 mg/kg) was injected intraperitoneally as an analgesic. Rats were deeply anesthetized with 4% isoflurane (mixed in oxygen and nitrous oxide at ratio 0.3/0.7) and anesthesia maintained at 2% isoflurane throughout the procedure. Body temperature and oxygen blood saturation/heart rate were monitored using a rectal probe and pulse oximeter, respectively, whereas the heating blanket was used to keep body temperature at $37 \pm 0.5^\circ\text{C}$.

2.6.3. Middle Cerebral Artery Occlusion (MCAo). Rats experienced temporary MCAo for 15 minutes ($n = 5$) and survived for 91 days. For MCA occlusion, a Buchan et al. [27, 28, 32] model was followed as a part of the research facility [27, 28, 33, 34] for the surgical ligation of tMCAo. This technique involved isolation of the left common carotid artery (LCCA) using loose ligation with silk 4–0. 2.5 cm skin incision was made between the lateral canthus of a right eye and external auditory canal to expose the temporalis muscle that was excised to approach the skull base. Craniectomy was performed, and LMCA was identified after dura retraction through a burr hole (2 mm). The desired position of MCA was sought to be at the point where it crossed the inferior cerebral vein, and a microaneurysm clip (number 1, Codman, Sundt AVM, Raynham, MA, USA) was applied proximal to this site so that the LCCA was ligated temporarily. After 15 minutes, the clip was removed and secure hemostasis was confirmed visually. The wound was closed at the end of the procedure. Later 91 days, the rats were beheaded; their brains were preserved overnight at 4°C in

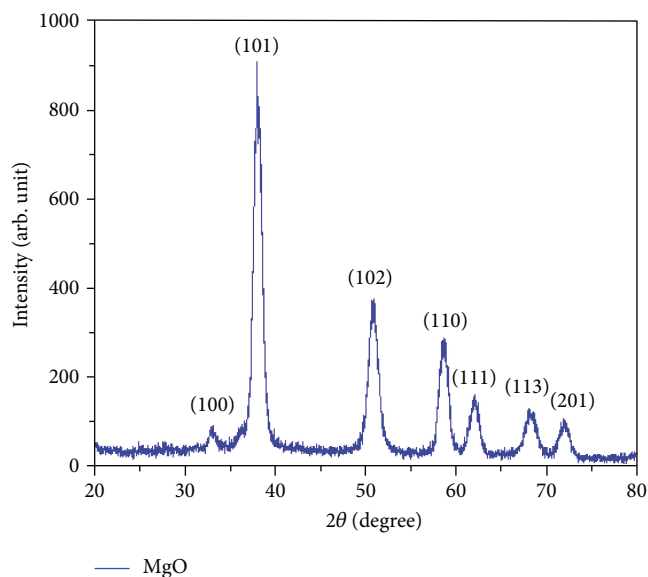


FIGURE 2: X-ray diffractogram of hydrated MgO.

4% PFA and then submersed in 0.1 M PBS containing 30% sucrose for 3–4 days. A sledge microtome was used to slice the harvested brains into sections with a thickness of 40 μm . Different sections were taken from the anterior forceps of the corpus callosum to the superior colliculi (Bregma 3.7 to 6.80 mm) and the visual cortex and fixed on gelatin-glazed slides [27, 28].

2.6.4. Post Procedure MRI. For MRI acquisition, 4% isoflurane mixed in 0.3 l/min oxygen and 0.7 l/min nitrous was supplied to a ventilator box in which each rat was kept at constant 37°C temperature. The inhalation was maintained with 1.5–2% isoflurane throughout the experiment. The adopted protocol was similar to the earlier reported [27, 29].

After 91 days, the postexposure images were obtained with a 4.7 T Magnetron (Bruker BioSpec 47/40 system; Bruker BioSpin GmbH, Ettlingen, Germany) with a 2 cm surface coil used for signal reception. T2-weighted images were taken at TR = 3500 ms, TE = 36 ms, ELT = 8, slice thickness = 1 mm, and plane resolution = 0.156 mm. Diffusion-weighted images (DWI) were acquired with an EPI sequence at TR = 3000 ms, TE = 35 ms, 35 directions $b = 1000 \text{ s}/\text{mm}^2$, slice thickness = 1.5 mm, and plane resolution = 0.312 mm.

2.6.5. Immunofluorescence Test. The chemicals used were xylene, DPX mountant, euthatal, methanol (MetOH), distilled water, 4% paraformaldehyde, phosphate-buffered saline (PBS), 0.2% Triton X-100 in Trizma base solution (TXTBS), 3% normal horse serum (NHS; S-2000; Vector Laboratories) in TXTBS, 5% normal goat serum (NGS; S-1000; Vector Laboratories) in TXTBS, and Trizma base (TB) and Trizma nonsaline (TN) solutions. For immunofluorescence (IF), biomarkers, that is, neuronal N (NeuN; 1:100; MAB377; Chemicon International), microglia (OX42; 1:400; MCA275R; Serotec Ltd.), and glial fibrillary acidic protein (GFAP; 1:500; G3893; Sigma-Aldrich

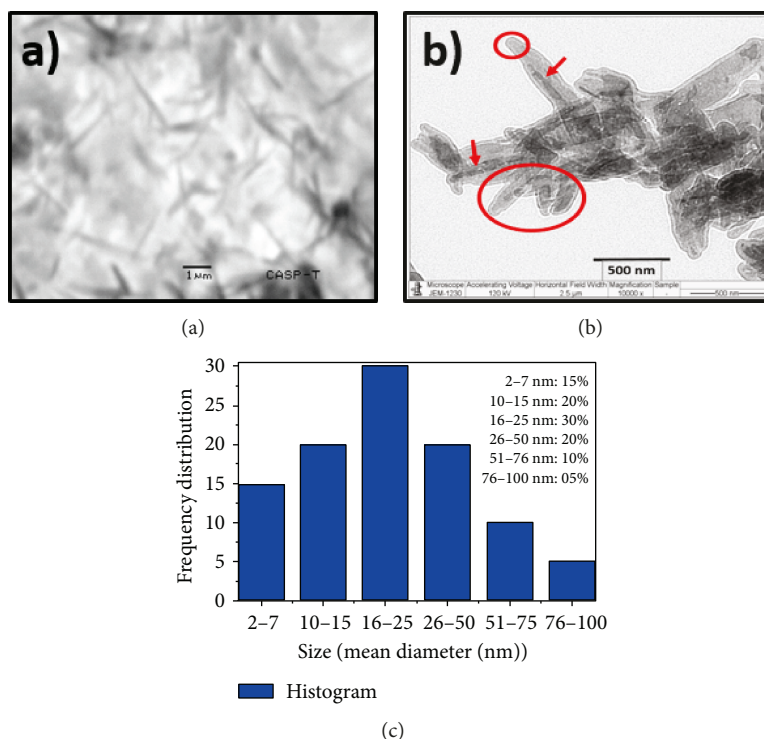


FIGURE 3: SEM (a) and TEM (b) micrographs of MgO nanotubes and (c) size distribution histogram.

company, Ltd.) as primary while goat anti-mouse Cy3 (1:150; Jackson ImmunoResearch) as secondary antibody media were prepared and utilized in the laboratory [27, 28]. Brain sections were quenched in a solution (10% MetOH and 10% H₂O₂) for 5 minutes and fixed in 3% NHS-PBS (for 2 hours) plus 5% NGS-PBS (for 2 hours) at room temperature. An approximately 2 ml mixture of nanoMgO and primary antibody specific to the nuclear protein for mature neurons (NeuN), reactive microglia and macrophages (OX42), and astrocytes (GFAP) was prepared in PBS, and the sections were incubated overnight (4°C) in the mixture. After being washed with TBS, the sections were further incubated in goat anti-mouse-Cy3 antibody at room temperature (2 hours). After 5 times washing, the sections were mounted on gelatin-coated slides, dried for 15 minutes on a heating block (40°C), and cover slipped using FluorSave reagent (Calbiochem) [27, 28].

3. Results and Discussion

The mode of crystallization and purity of experimentally calculated phases of synthesized powder sample were accessed with an X-ray diffractometer (2θ ranges (20–80°) at 40 kV, 40 mA with a ramp rate 0.02°) as shown in Figure 2. The obtained peaks of MgO with a hexagonal phase were completely affirmed with a PCPDFWIN card (07-0239). The maximum peak was used to calculate the average crystallite diameter < 10 nm by Debye's equation [35].

$$\text{Crystallite size} = 0.94 \frac{\lambda}{\beta} \text{WHM} \cos \theta, \quad (1)$$

where $\lambda = 1.54 \text{ \AA}$, is the wavelength of X-ray, FWHM is the broadening of the diffracted peak at the half maxima, and θ is the corresponding Bragg angle.

Figures 3(a)–3(c) display the structural architecture of MgO as recorded by a SEM and TE microscope. The SEM image describes needle-like structures (Figure 3(a)) at low magnification, indicating the formation of one-dimensional nanostructures of MgO. These needles grow asymmetrically and close to each other. Similarly, at high magnification (TEM), the image in the form of a tubular structure (Figure 3(b)) was observed which shows small and large agglomeration MgO NTbs. The graphical representation of the distribution of nanosized MgO as observed in the TE microscope at different size ranges (Figure 3(c)). TE microscopy was conducted to confirm that the particle size of MgO assessed from TEM images found was <50 nm. The histogram showed that maximum particles of the sample fall within the scope of 16–25 nm and mostly nanoparticles (above 75%) have a diameter less than 50 nm. This result is in close agreement with the particle size found by the Scherer formulae using XRD data.

TEM images (Figures 4(a) and 4(b)) confirmed the various morphologies (nanostars-NSTs and nanorods-NRs) of MgO obtained at annealing temperatures 250 and 350°C, respectively. The estimated sizes from TEM images were 30 nm and 12 nm in diameter and 80 nm in length of NSTs and NRs, respectively. It is believed that the synthesis parameters strongly influence the morphology and the particle size of the fabricated particles [36–39].

Phase composition of the as-prepared sample was determined by infrared spectroscopy. The observed peaks were

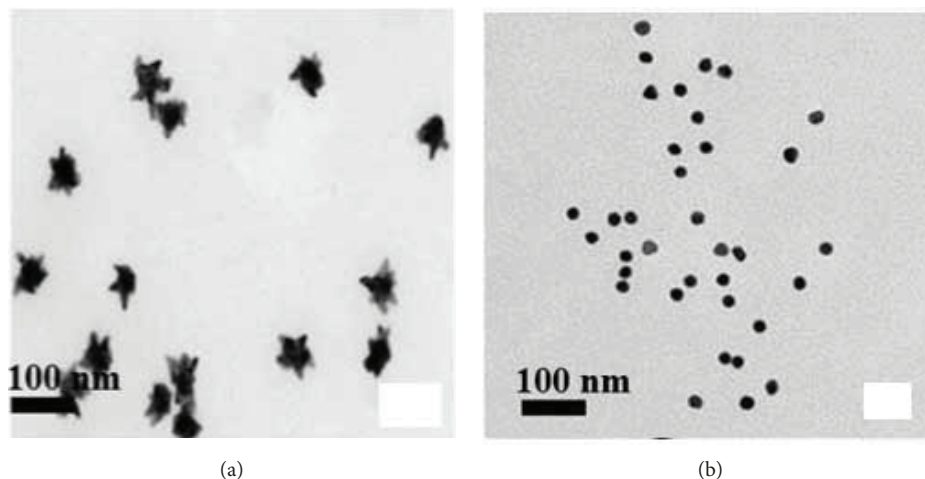


FIGURE 4: TEM images of MgO (a) nanostars at 350°C and (b) nanoparticles at 250°C.

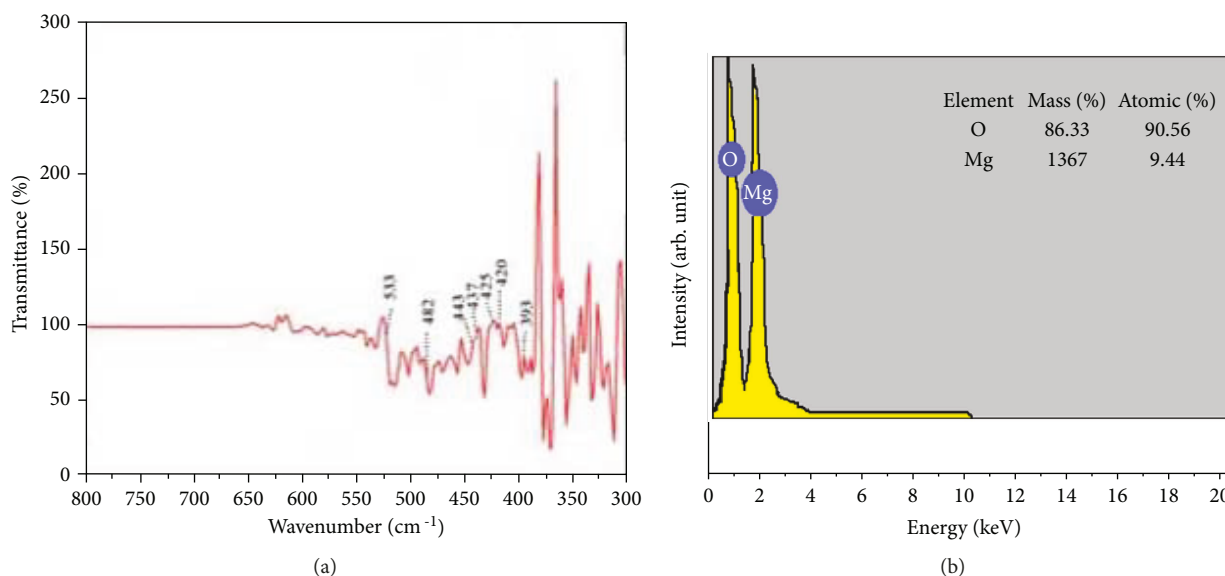


FIGURE 5: Bond variations and surface elemental composition in nanosized MgO performed by (a) FTIR spectroscopy and (b) EDX spectrum, respectively.

obtained over the frequency distribution ranging from 300 to 800 cm^{-1} , for MgO as shown in Figure 5(a) mostly reported. The maxima of the peaks appear at 393, 420, 425, and 443 cm^{-1} which have corresponded to the fundamental phonon MgO vibrations, and the characteristic band appeared at 437 cm^{-1} [40–44]. The peaks at 482 cm^{-1} and 533 cm^{-1} are associated to longitudinal optical phonon bands in MgO lattice [40, 45]. EDX also marks a major composite of oxygen (86.33) and magnesium (13.67) by mass (%) within the material (Figure 5(b)).

Raman and PL spectra of MgO NRs are presented in Figures 6(a) and 6(b). Raman peaks around 275.89, 442.15, and 1313.50 cm^{-1} (Figure 6(a)) are associated to the characteristics peaks of MgO and are found in good agreement with the previously reported research [46–49]. Generally, these bands are not present in the bulk MgO, so it confirms nanocrystalline phases within fabricated MgO [48] which is in concurrent to XRD analysis.

The luminescence spectrum of MgO (Figure 6(b)) showed multiple peaks around 383, 476, 573, 630, and 666 nm in the visible region [48, 50]. These emission peaks are attributed to the various structural defects, that is, internal stresses, oxygen vacancies, and presence of defects in/on a material surface, which may be produced during the conversion of $\text{Mg}(\text{OH})_2$ into MgO [48, 50]. The absence of PL emissions in the bulk MgO is also an evidence of the formation of MgO nanostructures which is consistent with the published results [22, 51, 52]. As a whole, the PL study confirms the formation of oxygen vacancies on the surface of nanostructured MgO.

The MgO NTs biodistribution results collected through liver, kidney, and brain sections of rats (group A) are investigated, and histopathological micrographs after 13 and 20 weeks are presented in (Figures 7(a)–7(f)). Skin and muscle data are not shown due to insignificant abnormalities as examined after pathology. The blood vessels were normal

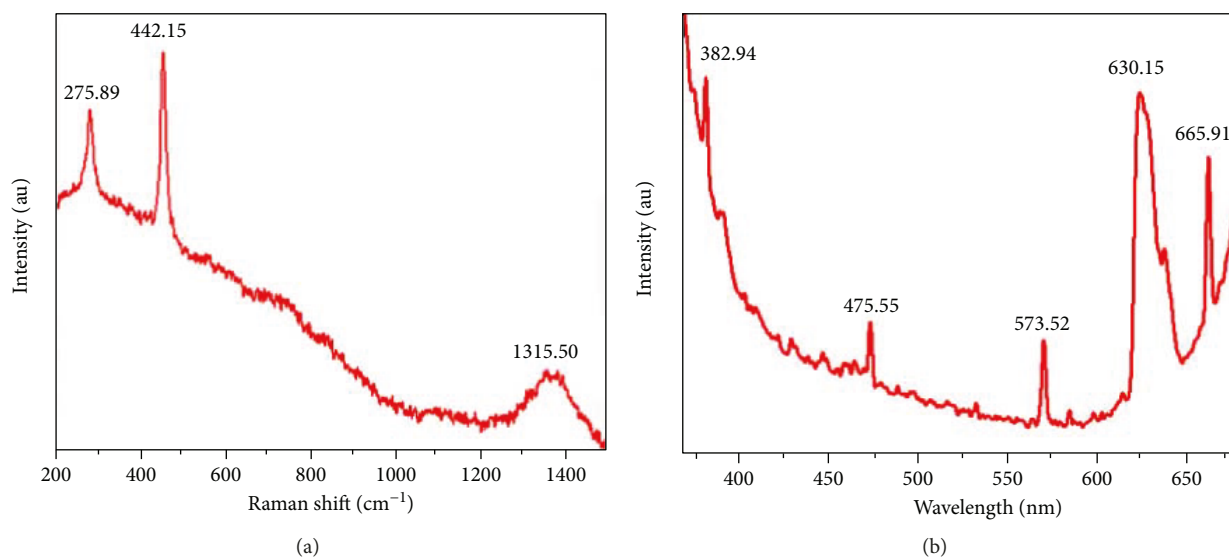


FIGURE 6: Raman spectrum (a) and PL profile (b) of MgO nanostructures.

while dermal layers, that is, the epidermis, dermis, and hypodermis were distinctly intact. Further, the structure of elastic fibers and collagen is slightly deformed. The intracellular toxicity induced by nanostructured MgO is depicted in Table 1.

Hematoxylin and Eosin (H&E) contrast was adopted to interpret the cellular structures. The cellular nuclei and the nuclear chromatin are in blue and purple-blue color; the cytosolic structures and red blood cells are in pink and in pink-red color while the morphological changes in the cell structures appeared as dark red/bright red. After 13 weeks, mild haemorrhages (arrow marked) were shown in the brain (Figure 7(a)), the liver displayed highly deterioration and congestion in hepatocytes and the marked areas show the foci of necrosis (Figure 7(b)), and severe renal tubular ablations (arrow marked) were observed in the kidney (Figure 7(c)). Some polymers and copolymers along with PEG, self-assembly micelles, and folic acid were reported for enhancing various cancer cell line drug uptakes, and a significant achievement has been found [53–57]. After 20 weeks, superficial congestions were seen in brain cells (Figure 7(d)), any remarkable deformities were not found in the liver (Figure 7(e)), and intense ablations and degenerations in renal tubules were found in the kidney (Figure 7(f)).

Statistical data analysis is required, in order to express the experimental data in some mathematical function which is helpful to show the effect of some trend in a quantitative manner. The statistical data of experiments are collected and analyzed with the help of the least square errors method as shown in Figure 8. It is observed that the exponential function is a natural selection for modeling the cell viability. The proposed model for “In Dark” and “Under 660 nm laser” is shown in (2) and (3), respectively. The values of all constants involved in the mathematical models are extracted using the least square error and shown after the equations. The single exponential function is not enough to imitate the experimental data as the rate of the change in cell viability for increasing MgO concentration which is initially large, whereas, at higher concentrations, the rate of change in cell viability is

less; therefore, there is a need of two exponential functions as modeled in (2) and (3). Furthermore, the decay constant of the “In Dark” model has a smaller value than the decay constant of “Under 660 nm laser” which shows the significant effects of laser on cell viability, in the first term of exponential. The first term of the exponential function will vanish for the larger values of MgO concentration, and there will be only the 2nd term left in both (2) and (3).

It can be seen that the decay constants for both “In Dark” and “Under 660 nm laser” in the second term of (2) and (3) are smaller relative to first term. Moreover, the decay constant of the second term in (3) is more than the decay constant of the second term in (1) which shows the significant effect of 660 nm laser on cell viability. Both the models shown in (2) and (3) are compared and found in coherence with the experimental data which validates the mathematical model as shown in Figure 8. Other parameters of fitness of the mathematical function are also shown in the following:

$$\text{In Dark} = a_1 * \exp(b_1 * x) + c_1 * \exp(d_1 * x), \quad (2)$$

where $a_1 = 5.064$, $b_1 = -0.02817$, $c_1 = 94.91$, $d_1 = -0.0004108$, and “ x ” is the MgO concentration ($\mu\text{g}\cdot\text{ml}^{-1}$) (SSE: 0.8483, R-square: 0.9969, adjusted R-square: 0.9923, and RMSE: 0.6513).

$$\text{Under 660 nm laser} = a_2 * \exp(b_2 * x) + c_2 * \exp(d_2 * x), \quad (3)$$

where $a_2 = 4.378$, $b_2 = -0.32$, $c_2 = 95.62$, $d_2 = -0.0007474$, and “ x ” is the MgO concentration ($\mu\text{g}\cdot\text{ml}^{-1}$) (SSE: 0.8483, R-square: 0.9969, adjusted R-square: 0.9923, and RMSE: 0.6513).

Similarly, four different experiments for cell viability were performed with various concentrations of MgO and are modeled as shown in Figure 9. All of the experimental data is analyzed using the method of the least square errors, and a mathematical expression is extracted using this data.

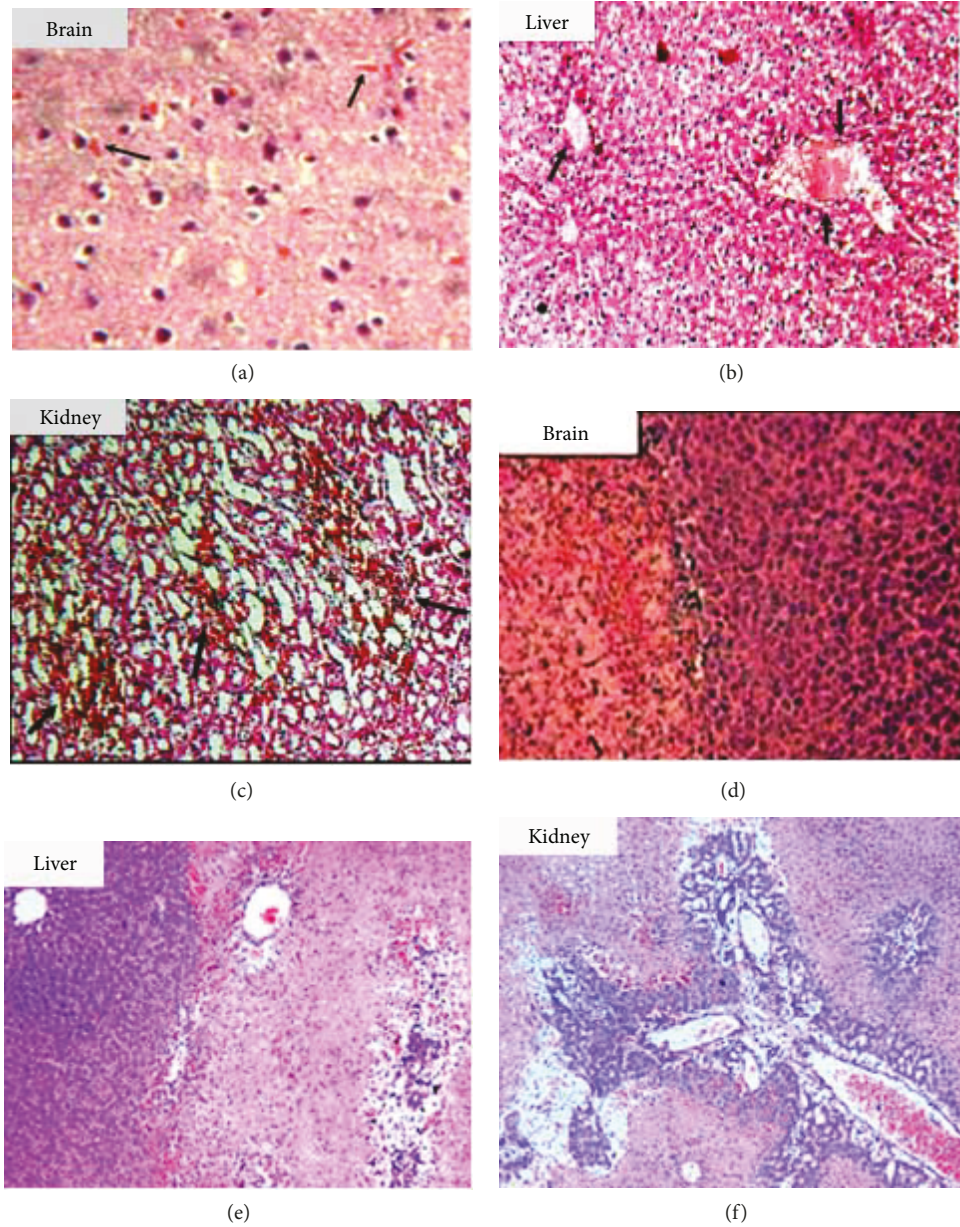


FIGURE 7: H&E contrasts of the cellular responses in different organs (brain, liver, and kidney) of rats when instilled by MgO NTbs after 13 and 20 weeks at 40x were shown in (a–c) and (d–f), respectively.

These curves are well-matched to the 3rd order polynomial with small values of the sum of the square of errors. Higher order polynomials will produce a lesser error at the cost of the complex mathematical model. However, the model, presented in Figure 9, is producing error less than 5% which is sufficient to validate any experimental data. It is also found that the cell viability is decreasing with the increase in concentration. The rate of the decrease in cell viability is the maximum for the MgO NRs and modeled with the suitable constants provided in (4) [58–60]. Similarly, all other experiments are modeled in (5), (6), and (7) after analysis and are presented in Figure 9.

$$\text{MgO NRs} = p_1 * x^3 + p_2 * x^2 + p_3 * x + p_4, \quad (4)$$

TABLE 1: Intracellular toxicity level of MgO in various vital organs.

Nanomaterial MgO (after weeks)	Skin	Muscle	Brain	Liver	Kidney
13	–	–	–	+	++
20	–	–	+	+	++

–: mild; +: moderate; ++: severe.

where $p_1 = -1.926e-06$, $p_2 = 0.0008937$, $p_3 = -0.1865$, and $p_4 = 99.87$ (SSE: 1.159, R-square: 0.9958, adjusted R-square: 0.9895, and RMSE: 0.7612).

$$\text{MgO NP} = p_{11} * x^3 + p_{21} * x^2 + p_{31} * x + p_{41}, \quad (5)$$

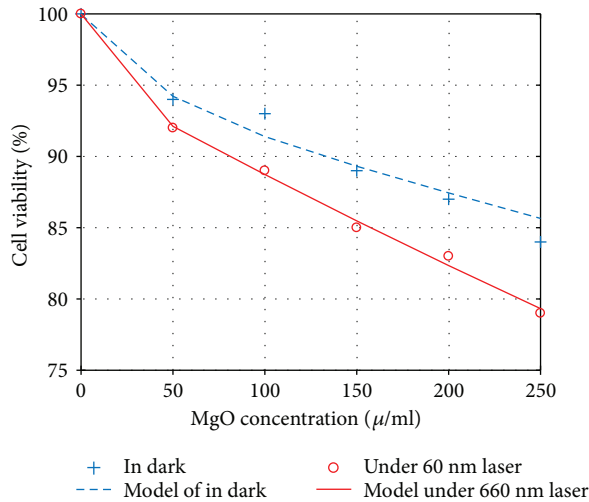


FIGURE 8: Mathematical model of cell viability (%) obtained from the experiments using various nanostructure data towards human glioblastoma cell lines (T98G) In Dark and Under 660 nm laser irradiation.

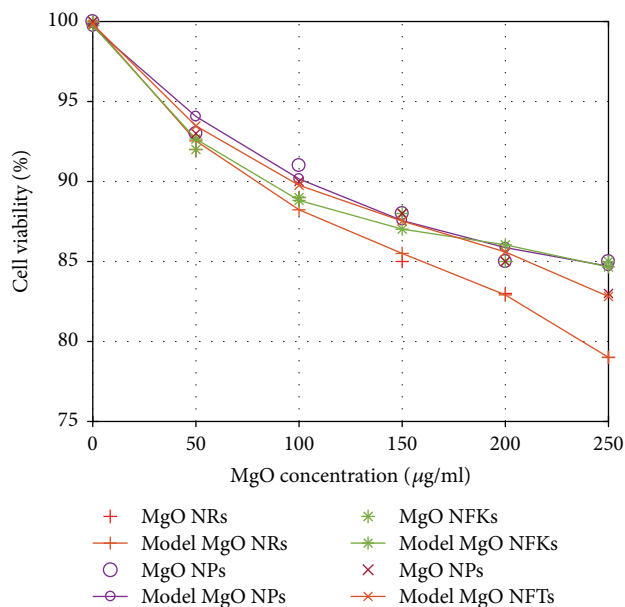


FIGURE 9: Mathematical model of cell viability (%) deduced from experiments using various nanostructures towards human glioblastoma cell lines (T98G).

where $p_{11} = -5.185e-07$, $p_{21} = 0.0004159$, $p_{31} = -0.1314$, and $p_{41} = 99.66$ (SSE: 2.992, R-square: 0.9817, adjusted R-square: 0.9542, and RMSE: 1.223).

$$\text{MgO NFKs} = p_{12} * x^3 + p_{22} * x^2 + p_{32} * x + p_{42}, \quad (6)$$

where $p_{12} = -1.63e-06$, $p_{22} = 0.0008968$, $p_{32} = -0.1827$, and $p_{42} = 99.75$ (SSE: 2.683, R-square: 0.9831, adjusted R-square: 0.9578, and RMSE: 1.158).

$$\text{MgO NFTs} = p_{13} * x^3 + p_{23} * x^2 + p_{33} * x + p_{43}, \quad (7)$$

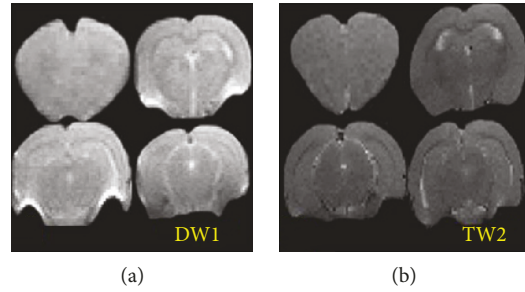


FIGURE 10: MRI after 15 minutes of occlusion.

where $p_{13} = -1.556e-06$, $p_{23} = 0.0007619$, $p_{33} = -0.1613$, and $p_{43} = 99.83$ (SSE: 0.9286, R-square: 0.995, adjusted R-square: 0.9876, and RMSE: 0.6814).

DWI and T2W images (Figure 10) showed no significant change in brain pathology after 91 days which supports that 15-minute occlusion just produced subtle neuroinflammations that cannot be detected in current MRI modalities. Thus, immunofluorescence assay was adopted to figure out specific bindings between antibodies tagged with nanotubes and antigens and the confinement of these neuroinflammations.

An immunofluorescence test was carried out to observe the localization of neuroinflammation by antibody nanomolecule. MgO nanomolecule showed variations in bonding patterns. Neurons were not appropriately labelled with this nanomolecule, though tagging with OX42 and GFAP was of slightest degree (Figure 11).

Many promising techniques still figured out several issues like limitations of reliable protocols such as appropriate labelling, interaction of hydrophobic and hydrophilic nanoparticles, and proper visibility of cells from data for disease recognition, to achieve a minimal damaging effect in a healthy site [61–64].

Superficial toxicity was counted in a rat skin, muscle, and brain tissues, but significant toxicity towards the liver and kidney was investigated. In the case of the brain cell model, results were nonsignificant too; about 17% toxicity was measured in the case of light and dark as well.

4. Conclusion

MgO nanostructures were successfully grown using a coprecipitation technique at different annealing temperatures. The different morphologies of crystalline MgO (NSTs and NTs, NRs) were found to depend upon annealing temperatures (250 and 350°C), respectively. The average calculated particle sizes (14 nm, 30 nm, and a diameter of ~10 nm and 12 nm) of samples from XRD are in good agreement with SEM and TEM. TEM images show the asymmetric growth of nanotubes in an agglomerated manner and homogeneous morphologies of NSPs, NSTs, and NRs. FTIR and EDX spectra show the presence of MgO in the fabricated powder. Raman and PL spectra also provide evidence that the nanostructured MgO is highly crystalline in nature. The inflammations which induced MgO were examined in vital organs (brain, liver, and kidney) of rats by H&E contrast which depicts

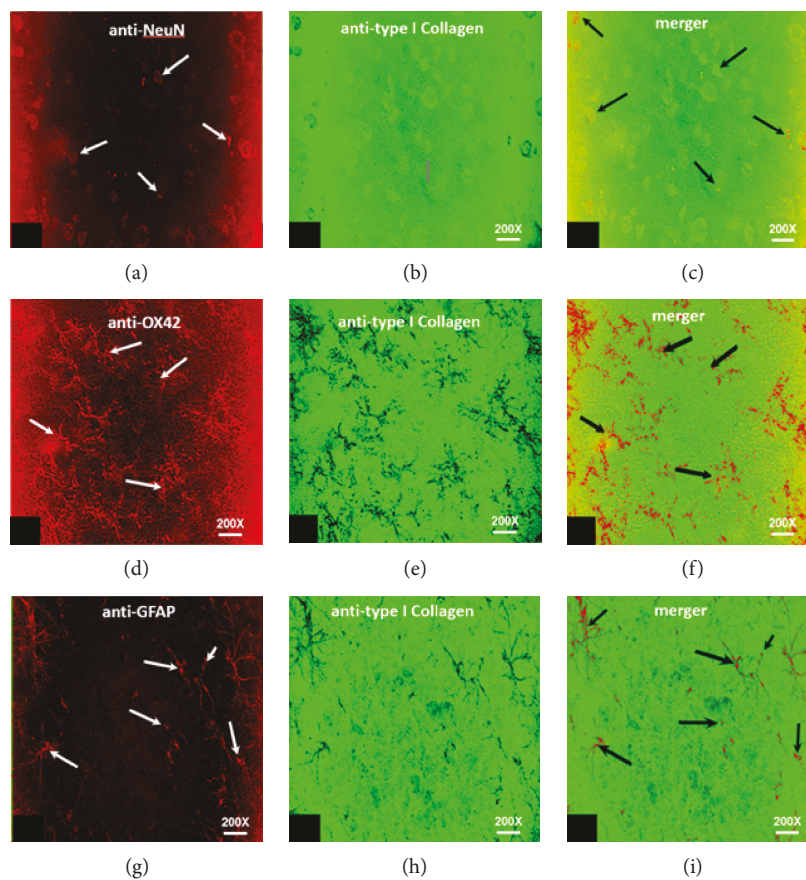


FIGURE 11: Rhodamine antibody IgG is used as a contrast agent for antibody-antigen linkage. The slides labelled as (a), (d), and (g) are the real micrograph obtained from confocal microscope, showing the linkage of MgO nanostructures with the respective neurons, microglia, and astrocytes in a rat brain. The slides (b), (e), and (h) labelled as anti-type I collagen are used as the green background to determine the cellular structure. The slides labelled as (c), (f), and (i) are the images produced by merging (a) to (b), (d) to (e), and (g) to (h) images obtained by computer-aided techniques which give a better contrast IF image.

the presence of nanostructures in the brain after 20 weeks rather than 13 weeks; however, the liver and kidney showed noxious inflammations in both intervals. Nanorods (1D) are significant than other morphologies exhibiting less toxicity (about 17% loss in cell viability) as recorded MTT assay applied to an *in vitro* model. No inflammations were detected in the rat brain MRI after 91 days induction of 15 min MCA occlusion. Furthermore, immunofluorescence analysis revealed inappropriate antibody-antigen bindings with MgO, while few incidences of bindings were observed with OX42 and GFAP. This paper describes the biodistribution of MgO and their specific antigen bindings in ischemic stroke, with an intention to produce chemically effective biocompatible materials, to develop and improve the treatments to revamp patients against ischemic stroke. However, more careful assessments are required for therapeutic purposes.

Conflicts of Interest

The authors declared no conflict of interest in this experimental work.

Acknowledgments

The authors would like to acknowledge the Higher Education Commission of Pakistan. They would like to thank the Department of Clinical Neurosciences, Cambridge University, UK, for financial support through IRSIP and “Indigenous Ph.D. Fellowship Program (5000 Fellowships).” Special thanks are given to Dr. Munir Ahmad (Nuclear Specialist, Institute of Nuclear Medicine and Oncology Lahore (INMOL), Lahore, Pakistan) and Mr. Khalid Rasheed Javed (Scientific Officer, Pakistan Council for Scientific and Industrial Research (PCSIR), Lahore, Pakistan) for their kind guidance in this research.

References

- [1] E. Silverman, M. M. Rymer, and L. R. Caplan, *An Atlas of Investigation and Treatment: Ischemic Stroke*, Atlas Medical Publishing Ltd., UK, 2009.
- [2] S. Bhaskar, F. Tian, T. Stoeger et al., “Multifunctional nanocarriers for diagnostics, drug delivery and targeted treatment across blood-brain barrier: perspectives on tracking and neuroimaging,” *Particle and Fibre Toxicology*, vol. 7, no. 1, p. 3, 2010.

- [3] M. A. Shah and A. Tokeer, *Principles of Nanoscience and Nanotechnology*, Narooosa Publishing House, India, 2010.
- [4] F. Lu, S. H. Wu, Y. Hung, and C. Y. Mou, "Size effect on cell uptake in well-suspended, uniform mesoporous silica nanoparticles," *Small*, vol. 5, no. 12, pp. 1408–1413, 2009.
- [5] H. C. Huang, S. Barua, G. Sharma, S. K. Dey, and K. Rege, "Inorganic nanoparticles for cancer imaging and therapy," *Journal of Controlled Release*, vol. 155, no. 3, pp. 344–357, 2011.
- [6] F. Alexis, E. Pridgen, L. K. Molnar, and O. C. Farokhzad, "Factors affecting the clearance and biodistribution of polymeric nanoparticles," *Molecular Pharmaceutics*, vol. 5, no. 4, pp. 505–515, 2008.
- [7] C. Martinez-Boubeta, L. Balcells, R. Cristòfol et al., "Self-assembled multifunctional Fe/MgO nanospheres for magnetic resonance imaging and hyperthermia," *Nanomedicine: Nanotechnology, Biology, and Medicine*, vol. 6, no. 2, pp. 362–370, 2010.
- [8] G. Rudramurthy, M. Swamy, U. Sinniah, and A. Ghasemzadeh, "Nanoparticles: alternatives against drug-resistant pathogenic microbes," *Molecules*, vol. 21, no. 7, p. 836, 2016.
- [9] Z. Bakhtiary, A. A. Saei, M. J. Hajipour, M. Raoufi, O. Vermesh, and M. Mahmoudi, "Targeted superparamagnetic iron oxide nanoparticles for early detection of cancer: possibilities and challenges," *Nanomedicine: Nanotechnology, Biology and Medicine*, vol. 12, no. 2, pp. 287–307, 2016.
- [10] S. Fütterer, I. Andrusenko, U. Kolb, W. Hofmeister, and P. Langguth, "Structural characterization of iron oxide/hydroxide nanoparticles in nine different parenteral drugs for the treatment of iron deficiency anaemia by electron diffraction (ED) and X-ray powder diffraction (XRPD)," *Journal of Pharmaceutical and Biomedical Analysis*, vol. 86, pp. 151–160, 2013.
- [11] M. A. Westwood, F. Shah, L. J. Anderson et al., "Myocardial tissue characterization and the role of chronic anemia in sickle cell cardiomyopathy," *Journal of Magnetic Resonance Imaging*, vol. 26, no. 3, pp. 564–568, 2007.
- [12] J. J. Brown, M. R. Hynes, and J. H. Wible Jr., "Measurement of serum calcium concentration after administration of four gadolinium-based contrast agents to human volunteers," *American Journal of Roentgenology*, vol. 189, no. 6, pp. 1539–1544, 2007.
- [13] D. R. Broome, M. S. Girguis, P. W. Baron, A. C. Cottrell, I. Kjellin, and G. A. Kirk, "Gadodiamide-associated nephrogenic systemic fibrosis: why radiologists should be concerned," *American Journal of Roentgenology*, vol. 188, no. 2, pp. 586–592, 2007.
- [14] E. Kanal, A. J. Barkovich, C. Bell et al., "ACR guidance document for safe MR practices: 2007," *American Journal of Roentgenology*, vol. 188, no. 6, pp. 1447–1474, 2007.
- [15] P. H. Kuo, E. Kanal, A. K. Abu-Alfa, and S. E. Cowper, "Gadolinium-based MR contrast agents and nephrogenic systemic fibrosis," *Radiology*, vol. 242, no. 3, pp. 647–649, 2007.
- [16] G. Duan, X. Yang, J. Chen, G. Huang, L. Lu, and X. Wang, "The catalytic effect of nanosized MgO on the decomposition of ammonium perchlorate," *Powder Technology*, vol. 172, no. 1, pp. 27–29, 2007.
- [17] H. Niu, Q. Yang, K. Tang, and Y. Xie, "Self-assembly of porous MgO nanoparticles into coral-like microcrystals," *Scripta Materialia*, vol. 54, no. 10, pp. 1791–1796, 2006.
- [18] K. R. Javed, M. Ahmad, S. Ali et al., "Comparison of doxorubicin anticancer drug loading on different metal oxide nanoparticles," *Medicine*, vol. 94, no. 11, article e617, 2015.
- [19] M. Fresta, G. Puglisi, G. Giammona, G. Cavallaro, N. Micali, and P. M. Furneri, "Pefloxacin mesilate- and ofloxacin-loaded polyethylcyanoacrylate nanoparticles: characterization of the colloidal drug carrier formulation," *Journal of Pharmaceutical Sciences*, vol. 84, no. 7, pp. 895–902, 1995.
- [20] F. Forestier, P. Gerrier, C. Chaumanrd, A. M. Quero, P. Couvreur, and C. Labarre, "Effect of nanoparticle-bound ampicillin on the survival of *Listeria monocytogenes* in mouse peritoneal macrophages," *Journal of Antimicrobial Chemotherapy*, vol. 30, no. 2, pp. 173–179, 1992.
- [21] Z. Cui, G. W. Meng, W. D. Huang, G. Z. Wang, and L. D. Zhang, "Preparation and characterization of MgO nanorods," *Materials Research Bulletin*, vol. 35, no. 10, pp. 1653–1659, 2000.
- [22] H. Kim, S. H. Shim, and L. Chongmu, "Temperature-controlled synthesis of MgO nanorods," *Journal of the Korean Physical Society*, vol. 49, pp. 628–631, 2006.
- [23] P. K. Stoimenov, R. L. Klinger, G. L. Marchin, and K. J. Klabunde, "Metal oxide nanoparticles as bactericidal agents," *Langmuir*, vol. 18, no. 17, pp. 6679–6686, 2002.
- [24] T. Jintakosol and P. Singjai, "Effect of annealing treatment on luminescence property of MgO nanowires," *Current Applied Physics*, vol. 9, no. 6, pp. 1288–1292, 2009.
- [25] M. Waseem Akram, M. Fakhar-e-Alam, M. Atif et al., "In vitro evaluation of the toxic effects of MgO nanostructure in Hela cell line," *Scientific Reports*, vol. 8, no. 1, article 4576, 2018.
- [26] W. Ma, A. Xu, J. Ying, B. Li, and Y. Jin, "Biodegradable core-shell copolymer-phospholipid nanoparticles for combination chemotherapy: an *in vitro* study," *Journal of Biomedical Nanotechnology*, vol. 11, no. 7, pp. 1193–1200, 2015.
- [27] A. R. Butt, S. Ejaz, J. C. Baron, M. Ikram, and S. Ali, "CaO nanoparticles as a potential drug delivery agent for biomedical applications," *Digest Journal of Nanomaterials and Biostructures*, vol. 10, pp. 799–809, 2015.
- [28] A. R. Butt, I. A. Butt, A. Nazir et al., "Molecular imaging of CaO nanowhiskers in living organs," *The Nucleus*, vol. 52, pp. 159–164, 2015.
- [29] S. Ejaz, D. J. Williamson, T. Ahmed et al., "Characterizing infarction and selective neuronal loss following temporary focal cerebral ischemia in the rat: a multi-modality imaging study," *Neurobiology of Disease*, vol. 51, pp. 120–132, 2013.
- [30] J. R. Peng, T. T. Qi, J. F. Liao et al., "Mesoporous magnetic gold "nanoclusters" as theranostic carrier for chemo-photothermal co-therapy of breast cancer," *Theranostics*, vol. 4, no. 7, pp. 678–692, 2014.
- [31] J. F. Liao, W. T. Li, J. R. Peng et al., "Combined cancer photothermal-chemotherapy based on doxorubicin/gold nanorod-loaded polymersomes," *Theranostics*, vol. 5, no. 4, pp. 345–356, 2015.
- [32] A. M. Buchan, D. Xue, and A. Slivka, "A new model of temporary focal neocortical ischemia in the rat," *Stroke*, vol. 23, no. 2, pp. 273–279, 1992.
- [33] J. L. Hughes, J. S. Beech, P. S. Jones, D. Wang, D. K. Menon, and J. C. Baron, "Mapping selective neuronal loss and microglial activation in the salvaged neocortical penumbra in the rat," *NeuroImage*, vol. 49, no. 1, pp. 19–31, 2010.
- [34] M. Takasawa, J. S. Beech, T. D. Fryer et al., "Imaging of brain hypoxia in permanent and temporary middle cerebral artery

- occlusion in the rat using ^{18}F -fluoromisonidazole and positron emission tomography: a pilot study," *Journal of Cerebral Blood Flow & Metabolism*, vol. 27, no. 4, pp. 679–689, 2006.
- [35] B. D. Cullity and S. R. Stock, *Elements of X-ray Diffraction*, Addison-Wesley Publishing Company, Publishikg Company, Inc., Boston, MA, USA, 3rd edition, 1956.
- [36] A. S. Fernandez, L. S. Gomez-Villalba, L. Muñoz, G. Flores, R. Fort, and M. E. Rabanal, "Effect of temperature and reaction time on the synthesis of nanocrystalline brucite," *International Journal of Modern Manufacturing Technologies*, vol. 6, pp. 50–54, 2014.
- [37] D. Xue, X. Yan, and L. Wang, "Production of specific $\text{Mg}(\text{OH})_2$ granules by modifying crystallization conditions," *Powder Technology*, vol. 191, no. 1-2, pp. 98–106, 2009.
- [38] Y. Liu, J. Liu, Y. Li, D. Wang, L. Ren, and K. Zou, "Effect of annealing temperature on the structure and properties of vanadium oxide films," *Optical Materials Express*, vol. 6, no. 5, pp. 1552–1560, 2016.
- [39] T. D. Malevu and R. O. Ocaya, "Effect of annealing temperature on structural, morphology and optical properties of ZnO nano-needles prepared by zinc air cell system method," *International Journal of Electrochemical Science*, vol. 10, pp. 1752–1761, 2015.
- [40] C. V. Raman, "Evaluation of Its Specific Heat, in the Vibrations of the MgO Crystal Structure and Its Infra-Red Absorption Spectrum," in *Proceedings of the Indian Academy of Sciences*, C. V. Raman, Ed., vol. A54, pp. 244–252, Bangalore, India, 1961.
- [41] C. V. Raman, "Dynamical Theory, in the Vibrations of the MgO Crystal Structure and Its Infra-Red Absorption Spectrum," in *Proceedings of the Indian Academy of Sciences - Section A*, C. V. Raman, Ed., vol. 54, pp. 223–232, Bangalore, India, 1961.
- [42] M. F. Parveen, S. Umopathy, V. Dhanalakshmi, and R. Anbarasan, "Synthesis and characterization of nanosized $\text{Mg}(\text{OH})_2$ and its nanocomposite with poly (vinyl alcohol)," *NANO*, vol. 4, no. 3, pp. 147–156, 2009.
- [43] S. P. Prabhavathi, Ranjith, S. Rajam, Maruthamuthu, and K. Raja, "Sol-Gel method of synthesis of MgO and CaO nanoparticles and their characterization," *World Journal of Pharmaceutical Research*, vol. 3, p. 362, 2014.
- [44] S. Balamurugan, L. Ashna, and P. Parthiban, "Synthesis of nanocrystalline MgO particles by combustion followed by annealing method using hexamine as a fuel," *Journal of Nanotechnology*, vol. 2014, Article ID 841803, 6 pages, 2014.
- [45] S. Makhluif, R. Dror, Y. Nitzan, Y. Abramovich, R. Jelinek, and A. Gedanken, "Microwave-assisted synthesis of nanocrystalline MgO and its use as a bactericide," *Advanced Functional Materials*, vol. 15, no. 10, pp. 1708–1715, 2005.
- [46] K. Ishikawa, N. Fujima, and H. Komura, "First order Raman scattering in MgO microcrystals," *Journal of Applied Physics*, vol. 57, no. 3, pp. 973–975, 1985.
- [47] H. S. Kim and H. W. Kim, "Fabrication and Raman studies of MgO/SnO_2 core-shell heteronanowires," *Acta Physica Polonica A*, vol. 116, no. 1, pp. 58–61, 2009.
- [48] K. Krishnamoorthy, J. Y. Moon, H. B. Hyun, S. K. Cho, and S.-J. Kim, "Mechanistic investigation on the toxicity of MgO nanoparticles toward cancer cells," *Journal of Materials Chemistry*, vol. 22, no. 47, pp. 24610–24617, 2012.
- [49] N. Awwad, A. Alshahrani, K. Saleh, and M. Hamdy, "A novel method to improve the anticancer activity of natural-based hydroxyapatite against the liver cancer cell line HepG2 using mesoporous magnesia as a micro-carrier," *Molecules*, vol. 22, no. 12, p. 1947, 2017.
- [50] L. Kumari, W. Z. Li, C. H. Vannoy, R. M. Leblanc, and D. Z. Wang, "Synthesis, characterization and optical properties of $\text{Mg}(\text{OH})_2$ micro-/nanostucture and its conversion to MgO," *Ceramics International*, vol. 35, no. 8, pp. 3355–3364, 2009.
- [51] Y. Hao, G. Meng, C. Ye, X. Zhang, and L. Zhang, "Kinetics-driven growth of orthogonally branched single-crystalline magnesium oxide nanostructures," *Journal of Physical Chemistry B*, vol. 109, no. 22, pp. 11204–11208, 2005.
- [52] G. H. Rosenblatt, M. W. Rowe, G. P. Williams, R. T. Williams, and Y. Chen, "Luminescence of F and F^+ centers in magnesium oxide," *Physical Review B*, vol. 39, no. 14, pp. 10309–10318, 1989.
- [53] Y. L. Lo, P. C. Lo, C. C. Chiu, and L. F. Wang, "Folic acid linked chondroitin sulfate-polyethyleneimine copolymer based gene delivery system," *Journal of Biomedical Nanotechnology*, vol. 11, no. 8, pp. 1385–1400, 2015.
- [54] S. Xiao, R. Castro, J. Rodrigues, X. Shi, and H. Tomás, "PAMAM dendrimer/pDNA functionalized-magnetic iron oxide nanoparticles for gene delivery," *Journal of Biomedical Nanotechnology*, vol. 11, no. 8, pp. 1370–1384, 2015.
- [55] H. Xu, C. Cai, J. Gou et al., "Self-assembled monomethoxy (polyethylene glycol)- b - $P(D,L$ -lactic- co -glycolic acid)- b - $P(L$ -glutamic acid) hybrid-core nanoparticles for intracellular pH-triggered release of doxorubicin," *Journal of Biomedical Nanotechnology*, vol. 11, no. 8, pp. 1354–1369, 2015.
- [56] R. Kumaran, Y. K. Choi, V. Singh et al., "In vitro cytotoxic evaluation of MgO nanoparticles and their effect on the expression of ROS genes," *International Journal of Molecular Sciences*, vol. 16, no. 12, pp. 7551–7564, 2015.
- [57] Q. Dong, S. Ge, Y. Shen et al., "Cytotoxic effects of MgO nanoparticles on human umbilical vein endothelial cells in vitro," *IET Nanobiotechnology*, vol. 5, no. 2, pp. 36–40, 2011.
- [58] T. K. Saito, M. Seki, and H. Tabata, "Self-organized ZnO nanorod with photooxidative cell membrane perforation enables large-scale cell manipulation," *Analytical and Bioanalytical Chemistry*, vol. 391, no. 7, pp. 2513–2519, 2008.
- [59] J. Li, D. Guo, X. Wang, H. Wang, H. Jiang, and B. Chen, "The photodynamic effect of different size ZnO nanoparticles on cancer cell proliferation in vitro," *Nanoscale Research Letters*, vol. 5, no. 6, pp. 1063–1071, 2010.
- [60] M. Fakhar-e-Alam, M. W. Akram, S. Iqbal et al., "Empirical modeling of physiochemical immune response of multilayer zinc oxide nanomaterials under UV exposure to melanoma and foreskin fibroblasts," *Scientific Reports*, vol. 7, article 46603, 2017.
- [61] M. Fakhar-e-Alam, M. U. Farooq, N. Abbas et al., "Pharmacokinetics and biodistribution of nickel oxide for liver cancer cure," *Journal of Optoelectronics and Advanced Materials*, vol. 18, pp. 414–418, 2016.
- [62] M. Fakhar-e-Alam, S. Rahim, M. Atif et al., "ZnO nanoparticles as drug delivery agent for photodynamic therapy," *Laser Physics Letters*, vol. 11, no. 2, article 025601, 2014.
- [63] M. Fakhar-e-Alam, S. Kishwar, and M. Willander, "Photodynamic effects of zinc oxide nanowires in skin cancer and fibroblast," *Lasers in Medical Science*, vol. 29, no. 3, pp. 1189–1194, 2014.
- [64] O. Betzer, R. Meir, T. Dreifuss et al., "In-vitro optimization of nanoparticle-cell labeling protocols for in-vivo cell tracking applications," *Scientific Reports*, vol. 5, no. 1, article 15400, 2015.



Hindawi
Submit your manuscripts at
www.hindawi.com

